

# PRS: Sharp Feature Priors for Resolution-Free Surface Remeshing

Natalia Soboleva<sup>1</sup> Olga Gorbunova<sup>1,3</sup> Maria Ivanova<sup>1,2</sup> Evgeny Burnaev<sup>1,2</sup>  
 Matthias Nießner<sup>4</sup> Denis Zorin<sup>5</sup> Alexey Artemov<sup>4</sup>

<sup>1</sup>Skolkovo Institute of Science and Technology <sup>2</sup>Artificial Intelligence Research Institute

<sup>3</sup>Yandex LLC <sup>4</sup>Technical University of Munich <sup>5</sup>New York University

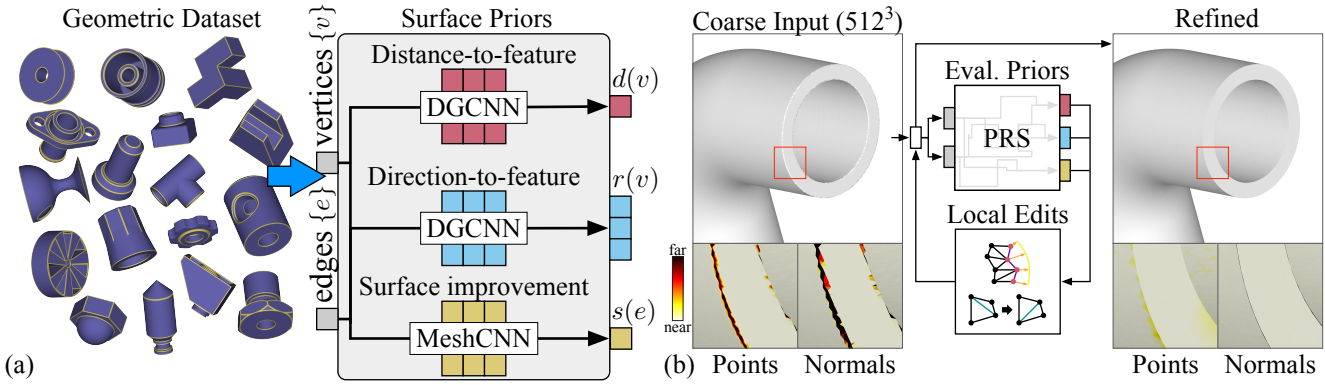


Figure 1. We use large volumes of geometric data to learn a collection of neural models sensitive to reconstruction accuracy of sharp geometric features (a), that we view as surface-based priors (PRS). We integrate our priors in an unstructured mesh editing algorithm for feature-aware remeshing of raw aliased mesh reconstructions, resulting in a faithful approximation of sharp geometric features (b).

## Abstract

Surface reconstruction with preservation of geometric features is a challenging computer vision task. Despite significant progress in implicit shape reconstruction, state-of-the-art mesh extraction methods often produce aliased, perceptually distorted surfaces and lack scalability to high-resolution 3D shapes. We present a data-driven approach<sup>1</sup> for automatic feature detection and remeshing that requires only a coarse, aliased mesh as input and scales to arbitrary resolution reconstructions. We define and learn a collection of surface-based fields to (1) capture sharp geometric features in the shape with an implicit vertexwise model and (2) approximate improvements in normals alignment obtained by applying edge-flips with an edgewise model. To support scaling to arbitrary complexity shapes, we learn our fields using local triangulated patches, fusing estimates on complete surface meshes. Our feature remeshing algorithm integrates the learned fields as sharp feature priors and optimizes vertex placement and mesh connectivity for maximum expected surface improvement. On a challenging collection of high-resolution shape reconstructions in the ABC dataset [43], our algorithm improves over state-of-the-art by 26% normals F-score and 42% perceptual RMSE<sub>v</sub>.

## 1. Introduction

Accurate 3D surface mesh models are commonly viewed as a desired final representation for 3D reconstruction; this view is supported by the prevalence of algorithmic and software tools that facilitate mesh manipulation. An important requirement for precise, high-quality surface reconstruction is preserving and explicitly representing sharp geometric features: perceptually, structurally, and functionally crucial regions present in many man-made shapes and explicitly stored in the CAD models [43, 51] but lost in raw meshes generated by 3D scanning devices or by iso-surfacing [35, 45, 50] volumetric representations.

Surface reconstruction with preservation of sharp geometric features has been approached from multiple directions, with notable improvements achieved in feature estimation [28, 51, 82], surface reconstruction [22, 87] and meshing [12, 13], or feature-preserving mesh smoothing [26, 65, 84, 93] and re-meshing [32]. However, most approaches come with practical limitations: they require access to additional information (e.g., clean 3D scans or accurate implicit functions), need manual, per-instance parameter tuning, or assume features to be already available (e.g. from prior estimation or user input). Many recent methods target iso-surfacing of implicit functions sampled on medium-size  $128^3$  grids and do not support high-resolution grids. As a result, despite substantial effort, reconstructing feature-equipped meshes remains a challenging task.

One promising path forward is to start with an initial, coarse mesh approximation constructed by an es-

<sup>1</sup>[artonson.github.io/publications/2024-prs](https://artonson.github.io/publications/2024-prs)

tablished procedure (e.g., [35, 45, 50]) and to iteratively refine it by applying standard local *remeshing* operations such as flipping edges and relocating vertices [1, 69] (for the example in the inset, performing six vertex moves and two edge-flips perfectly aligns the edges to a given curve).

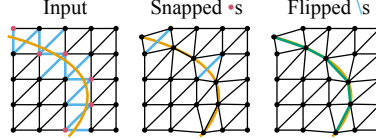
However, the detection of feature regions, selection of individual elements, and identification of parameters for each edit operation (e.g., deciding where to offset each vertex) all represent important challenges.

We argue that learning-based methods are a natural fit for such tasks as they can effectively leverage statistical patterns in large mesh datasets to predict improvements expected from applying editing operations in each location, thus serving as a form of surface priors for remeshing. In addition, they have the advantage of automatically adapting to individual input shapes without requiring per-model region-of-interest specification, supporting scaling to complex, high-resolution 3D models. Recent deep learning architectures operate directly on meshes or proxy graphs [24, 83], avoiding the need to involve any data other than the mesh itself.

In this paper, we propose an algorithm for refinement of triangle meshes designed to (1) automatically detect and reconstruct sharp geometric features in meshes, (2) require no user interaction for processing a particular input shape, (3) require no inputs other than triangle meshes, and (4) scale to 3D shapes meshed at arbitrary resolution. To satisfy these desiderata, we make a number of design decisions that we summarize below.

Our feature detection algorithm uses three fields defined at the elements of the input (coarse) surface mesh: two vertex-based fields encoding distances and normalized directions to the closest points on the feature curves, and an edge-based field capturing improvements in normal alignment obtained by flipping each edge, provided that all other remain fixed. We train three mesh-based neural networks to approximate each field. To scale our approach to complex 3D shapes, we learn all three fields on local triangulated patches; for reconstructing fields on a complete surface mesh, we fuse estimates from overlapping patches. We train our networks using a large-scale dataset of level-set meshes with realistic irregular chamfering and connectivity artifacts obtained from a simulated reconstruction process. For this purpose, we develop a training data generation pipeline based on high-quality, feature-equipped surface meshes in the ABC dataset [43].

Building on the three fields defined on complete 3D shapes, we develop an iterative algorithm integrating the fields as priors to achieve accurate feature reconstruction and remeshing. Specifically, in contrast to most mesh de-



noising methods, our remeshing algorithm optimizes *both vertex placement and edge connectivity* by snapping closest vertices to features and flipping edges with largest expected surface improvements. At each iteration, the procedure alternates evaluation of trained networks with local remeshing, checks predicted quantities against a threshold, and stops when expected gains in surface quality are small.

We benchmark our algorithm against state-of-the-art mesh extraction methods [12, 13, 42] and combinations of standard mesh extraction with feature-preserving denoising [65, 93], focusing on fine-grained feature reconstruction and surface quality measures. We additionally demonstrate how our algorithm complements smoothing methods, serving as a processing step in a reconstruction pipeline.

We contribute:

- An automatic method for estimating sharp geometric features and identifying surface meshing artifacts in 3D surface mesh models of arbitrary resolution, utilizing localized predictions and globally fusing local estimates.
- An automatic method for reconstructing and remeshing sharp geometric features in 3D surface meshes incorporating feature and surface improvement fields as priors for local surface remeshing.

## 2. Related Work

**Surface Reconstruction** is a central task in geometry processing [5, 31, 38]. Generating surfaces *explicitly*, e.g., by Delaunay triangulation of raw point sets [8, 19] or using recent neural network (NN)-based approaches [48, 62, 64] has limited use as these methods do not produce watertight, manifold structures needed by many applications.

*Implicit* reconstruction involves (1) fitting a scalar field to input points and (2) extracting its iso-surface as a mesh. A variety of methods including moving least squares regression [14, 56], Poisson surface reconstruction (PSR) [37], and deep kernel regression [86] are available for approximating scalar fields, each with trade-offs between robustness and detail preservation. Neural implicit fields, using NNs to represent the scalar field globally [53, 57], or locally [9, 33], improve fitting quality and scalability of implicit representations in many instances. For mesh extraction, all these approaches rely on the second ingredient of implicit reconstruction, iso-surfacing algorithms.

Iso-surfacing refers to approximating level sets of implicit functions (e.g., a signed distance field (SDF)). Traditionally, SDF values are sampled and analyzed in few individual, isolated locations such as vertices of cubes [50] or tetrahedra [23, 74]. Marching cubes (MC33) [15, 45, 50] enumerates sign configurations of the implicit field in vertices of a cube, defining the surface passing through points trilinearly interpolated on its edges. Such algorithms are local and straightforward to implement but lack guarantees on meeting feature preservation or mesh quality con-

ditions. Numerous improvements have been proposed in recent decades to address these limitations [12, 18, 54].

Relevant to this work, for preservation of sharp geometric features, several methods integrate alternative implicit representations (*e.g.*, distance gradients in addition to SDF values [35, 42]) or adaptive grid generation [61, 75]. These methods require explicitly defining features to generate an initial mesh. We experimentally compare to EMC [42].

Recently, Neural Marching Cubes (NMC) [12] and Neural Dual Contouring (NDC) [13] enhanced the triangulation algorithm with broader contextual information by training on a dataset of meshes. These methods lack scalability to 3D shapes sampled beyond the resolution they were trained for ( $128^3$ ). In contrast, our algorithm naturally processes meshes sampled at arbitrary resolution. We experimentally show that our feature-aware algorithm results in more accurate surface reconstruction, especially near features.

**Mesh Denoising** focuses on removing noise from vertex positions while retaining geometric features [4, 11, 68]. Many works adopt a two-step process, including filtering facet normals, often using a bilateral filter [96], and updating vertices to match denoised normals [71]. The effectiveness of the bilateral filter relies on the range kernel; constructing guidance normals was proposed through fitting quadrics [21, 80], bilateral filtering [89, 96], patch-based normal filtering [93], or non-local filtering [46, 84]. Recent data-driven mesh denoising methods learn guidance normals from training shapes [2, 65, 81, 94, 95].

Denoising per-vertex noise presumes that sharp features are present but corrupted by noise; this task is different from ours where features are irregularly triangulated and require reconstruction. As many denoising methods distort features when used in isolation [11], we demonstrate how one can complement these approaches using our feature-aware algorithm, integrating it with a two-stage denoising filter [93].

**Feature Detection.** Commonly, sets of mesh vertices are identified as instances of specific features (*e.g.*, sharp features, ridges, valleys, *etc.*). Estimating such features involves computing derivatives of principal curvature, a highly unstable computation for discrete, possibly noisy, surfaces [27, 36, 44, 90]. Methods with robustness to sampling and noise exist [39, 55, 73], but rely on proper feature reconstruction during mesh generation. Recent learning-based feature detection approaches operate directly on raw 3D scans [28, 49, 51, 82]; however, incorporating feature estimates in surface reconstructions has only seen few initial attempts [22, 87]. Our method reconstructs sharp features directly on meshes but does not expect features to form sequences of vertices [72], be directly sampled, or even belong to the surface. Instead, we view features as curves in 3D space, generally extending outside the model, and adopt an implicit feature representation similar to [51].

**Feature Remeshing** aims to improve the approximation of surface features in the mesh. Methods that extrapol-

late feature-adjacent smooth regions [3] or snap vertices to detected features [70, 77] were proposed. Recently, feature preservation has been shown via smooth, global mesh-field alignment [32, 60]. All these approaches require that features are supplied as input in some form. In contrast, our framework integrates automatic feature detection and remeshing in a unified algorithm.

## 3. Learning Sharp Feature Priors

### 3.1. Field Representations and Data Generation

We represent triangular meshes by a triple  $(V, F, E)$ , where  $V = \{v_i\}$  is the set of vertices, specified by their 3D coordinates, and  $F = \{f_j\}$  is the set of faces given by triples of indexes into  $V$ , and the set of edges  $E = \{e_k\}$ , given by vertex pairs.

**Feature-Equipped 3D Shapes.** Our source data is a subset of high-quality, feature-aligned 3D meshes provided in the ABC dataset [43], constructed by sampling and triangulating parametric boundary representations (B-Rep)s of the source CAD shapes, and providing vertexwise sharp feature annotations obtained by thresholding differences in analytic normals in smooth adjacent CAD regions in the B-Rep.

**Construction of Coarse 3D Meshes.** Per-vertex noise [47, 65] or random edge flips [24] do not model well surface reconstruction flaws such as irregular chamfering of sharp features [1]. Instead, we simulate a simplified reconstruction process for obtaining realistic mesh extraction artifacts. We build a volumetric SDF with voxel size  $\lambda$  by querying point-to-surface distances from each grid point of a regular 3D voxel grid to the ground-truth (GT) mesh and extract its level set using MC33 [45, 50] as the coarse mesh. To model unknown orientation, each GT mesh is randomly rotated before computing the SDF. Unlike methods assuming a fixed grid resolution (*e.g.*,  $64^3$  [12, 13]), we adapt the resolution of the volumetric grid to the complexity of the GT mesh, scaling it to sample feature curves of characteristic linear size with at least  $n$  points. We prune narrow triangles and remove excess vertices by collapsing short edges of length  $\alpha_{\text{short}}\lambda$  or smaller. Memory requirements are bounded by pre-selecting a set of models in ABC that yield volumetric grids of up to  $512^3$  voxels. We view  $512^3$  as coarse despite high voxel resolution due to aliasing artefacts (see explanation in Figure 4).

**Mesh Correspondence Maps.** To compute edge- and vertex-based fields, we transfer feature- and surface-aware annotations to the coarse mesh by constructing two correspondence maps between the faces of the GT and the newly constructed coarse surfaces. The coarse-to-GT map ( $\pi_{c \rightarrow g}$ ) is computed by uniformly sampling the coarse mesh and finding faces on the GT mesh closest to each sample. Swapping the two meshes yields the GT-to-coarse map ( $\pi_{g \rightarrow c}$ ). Bidirectional mapping accurately handles instances of differences in face sizes between the two meshes.

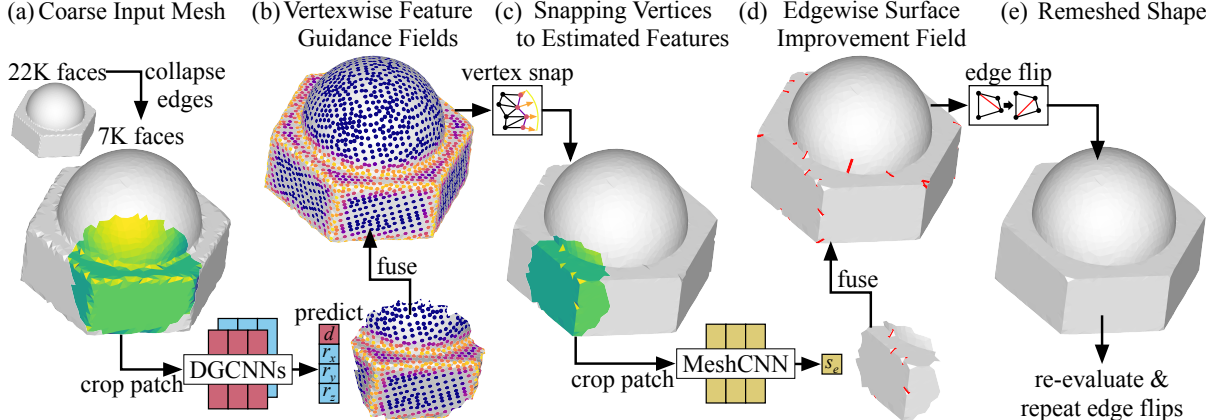


Figure 2. We start with an coarse input mesh that we decimate by collapsing short edges (a). To detect poorly meshed near-feature regions, we crop local triangulated mesh patches, predict patch-level distance- and direction-to-feature fields (1) and integrate these into an object-level field (b); we use this field to snap near-feature vertices onto predicted feature curves (c). To further improve feature meshing, we iteratively detect edges with large potential surface improvement (3) and flip these (d–e). Mesh integrity is maintained at each stage.

**Patch and Feature Selection.** As training with detailed 3D meshes is impractical and is likely to generalize poorly, we train on a set of local mesh patches, constraining the complexity of training instances and enabling handling of arbitrarily large models. For a coarse surface, we sample up to 1K uniformly distributed seed points, cut out connected sub-meshes within the distance  $\alpha_{\text{patch}}\lambda$  to each seed, and retrieve their feature-equipped counterparts from the GT mesh using  $\pi_{c \rightarrow g}$ . We keep interior sharp features (*i.e.*, those passing through non-boundary edges in the GT patch) and eliminate the rest.

**Distance- and Direction-to-Feature Fields.** Following a recent feature estimation approach [51], we implicitly represent features using the scalar *distance-to-feature* field  $d^\varepsilon(v)$  and the vector *direction-to-feature* field  $r^\varepsilon(v)$ , defining these at vertices  $v \in V$  in the coarse mesh. We truncate both fields at a radius  $\varepsilon$ , a multiple of the sampling distance  $\lambda$  (choosing  $\varepsilon = 4\lambda$ ). To compute these quantities at a vertex  $v$ , we map  $v$  to its closest neighbor  $q(v)$  belonging to the feature curves in the GT mesh and set

$$\begin{aligned} d^\varepsilon(v) &= \min(|q(v) - v|, \varepsilon) \\ r^\varepsilon(v) &= \text{normalize}(q(v) - v) \cdot \mathbb{I}(d^\varepsilon(v) < \varepsilon). \end{aligned} \quad (1)$$

where  $\mathbb{I}$  denotes the indicator function. The field  $r^\varepsilon$  contains unit-length direction vectors for points closer to features than  $\varepsilon$ , and zeros elsewhere.

**Surface Improvement Field** captures changes in normals alignment between the coarse and the GT meshes resulting from an isolated edge-flip. We start by defining a scalar surface normal consistency (NC) measure by integrating deviation between the coarse normal  $n_{\text{crs}}(f)$  and GT normals sampled in matching (under  $\pi_{c \rightarrow g}$ ) locations:

$$\text{nc}(f) = \frac{1}{|f|} \int_f \|n_{\text{crs}}(u) - n_{\text{gt}}(\pi_{c \rightarrow g}(u))\| du. \quad (2)$$

Edge-based normals consistency  $\text{nc}(e)$  is given by weighted

averaging  $\text{nc}(e) = w_1 \text{nc}(f_1) + w_2 \text{nc}(f_2)$  of the two face-based values  $\text{nc}(f_{1,2})$  incident at  $e$ . Finally, our edgewise surface improvement field is given by the difference

$$s(e) = \text{nc}(e') - \text{nc}(e), \quad e \in E, \quad (3)$$

where  $\text{nc}(e')$  refers to the NC of the flipped edge  $e'$ .

### 3.2. Patch-Based Field Estimation and Fusion

We learn signals directly on triangular meshes, without resorting to regular representations (*e.g.*, voxelization or sampling). We introduce three mesh-based deep networks  $f_d$ ,  $f_r$ , and  $f_s$  for regressing distance-to-feature, direction-to-feature, and surface improvement fields, respectively.

**Distance- and Direction-to-Feature Fields.** We define our deep estimators of distance- and direction-to-feature fields at vertices  $V$  in the coarse mesh. Architecturally, our models are generalized variants of the DGCNN [83]. We find the optimal learning configuration by experimenting with hyperparameters summarized in Tab. 1. The distance-to-feature model optimizes a combination of  $L_2$  and Laplacian terms emphasizing accurate, smooth predictions for vertices closest to the sharp features:

$$L(d^\varepsilon, \hat{d}^\varepsilon) = L_2(\log d^\varepsilon, \log \hat{d}^\varepsilon) + 0.1 L_{\text{lap}}(d^\varepsilon, \hat{d}^\varepsilon), \quad (4)$$

In this equation, the Laplacian smoothing term is

$$L_{\text{lap}}(d^\varepsilon, \hat{d}^\varepsilon) = (\Delta d^\varepsilon - \Delta \hat{d}^\varepsilon)^2, \quad (5)$$

where the Laplacian of  $d^\varepsilon$  can be computed by

$$(\Delta d^\varepsilon)(v) = \frac{1}{Z} \sum_{u \in N(v)} L_{vu} d^\varepsilon(u) - d^\varepsilon(v). \quad (6)$$

Here  $Z = \sum_{u \in N(v)} L_{vu}$  is the normalizing constant,  $N(v)$  is the set of vertices adjacent to  $v$ , and  $L_{vu}$  is the discrete

	#P	In.	Out.	Losses	#P/f.	Coll.	Rec.( $\lambda$ )↑	FPR( $\lambda$ )↓	$F_{\infty}\uparrow$	$FN_{\infty}\uparrow$
distances-to-feature	* 2K	$v$	$d$	$\log L_2 + \text{Lap}$	80	1	<b>98.2</b>	0.57	<b>96.1</b>	98.6
	500	$v$	$d$	$\log L_2 + \text{Lap}$	80	1	72.0	0.55	93.4	<b>98.7</b>
	500	$v, n_v$	$d$	$\log L_2 + \text{Lap}$	80	1	70.5	<b>0.27</b>	<b>93.5</b>	98.6
	500	$v$	$d$	$\log L_2$	80	1	71.9	0.43	93.4	98.6
	500	$v$	$d$	$L_2$	80	1	71.6	0.54	93.2	98.4
	500	$v$	$d, r$	$L_2$	80	1	67.5	0.97	92.1	97.3
	500	$v, n_v$	$d$	$\log L_2 + \text{Lap}$	80	0	34.2	<b>0.32</b>	87.8	<b>98.9</b>
	500	$v, n_v$	$d$	$\log L_2 + \text{Lap}$	80	0.5	56.8	0.38	91.6	<b>98.9</b>
	500	$v, n_v$	$d$	$\log L_2 + \text{Lap}$	8	1	<b>91.1</b>	1.39	84.8	89.6
directions-to-feature	* 2K	$v$	$r$	$L_2$	80	1	<b>94.9</b>	<b>5.1</b>	<b>96.0</b>	<b>98.7</b>
	500	$v$	$r$	$L_2$	80	1	67.8	32.2	<b>93.2</b>	98.5
	500	$v, n_v$	$r$	$L_2$	80	1	67.3	32.7	<b>93.2</b>	<b>98.5</b>
	500	$v$	$d, r$	$L_2$	80	1	68.0	32.0	92.1	97.3
	500	$v, n_v$	$r$	$L_2$	8	1	<b>80.0</b>	<b>20.0</b>	83.4	89.0

Table 1. Quantitative comparison of various learning configurations for estimating distance (*top*) and direction (*bottom*) fields. #P: number of vertices, Inputs (In.): vertices ( $v$ ), vertex normals  $n_v$ , Outputs (Out.): distances ( $d$ ), directions ( $r$ ), #P/f.: points per feature, Collapses (Coll.): ratio of collapsed edges (Sec. 3.1).

cotangent Laplacian (see, *e.g.*, [16]). Our directions-to-feature estimator minimizes  $L_2$  loss for vertices.

**Surface Improvement Field.** We define our deep surface improvement estimator at the edges  $E$  of the coarse patches and uses these predictions for edge flips during remeshing. We use the edge-based MeshCNN network [24], modifying it to perform fewer poolings (1.2K vertices) to avoid collapsing boundary edges. We train our network using the binary cross-entropy loss to predict surface improvement values  $s(e)$  exceeding the threshold  $\alpha_s = 0.1$ .

**Fusion of Per-Patch Predictions.** We reconstruct the three fields  $\hat{d}, \hat{r}, \hat{s}$  on complete 3D meshes from local patch-based predictions. Patches outside feature regions are excluded if  $q_{\alpha}(\hat{d}_i) > \lambda/2$  where  $q_{\alpha}(\hat{d}_i)$  represents the  $\alpha$ -quantile of values in  $\hat{d}_i$  (we use  $\alpha = 10\%$ ). Multiple predictions in each vertex are correlated due to overlapping patches. We use a statistical algorithm for averaging correlated predictions [63], involving computing weighted averages of field values in each element in the mesh.

## 4. Mesh Refinement

**Overview.** Our remeshing method iteratively optimizes vertex locations and face orientations to reconstruct cleaner sharp geometric features. We use standard remeshing operations, *vertex repositioning* and *edge flips* (see [6, 30]). The application of these operations is guided by fields predicted by our neural networks. Additionally, we incorporate *edge and face collapses* [29] as preliminary steps to simplify input meshes and match the training data distribution. To mitigate undesired effects during the remeshing process – such as abrupt flips in face normals or manifoldness violations – we establish and maintain a set of invariants. These invariants are checked for each modified element, following

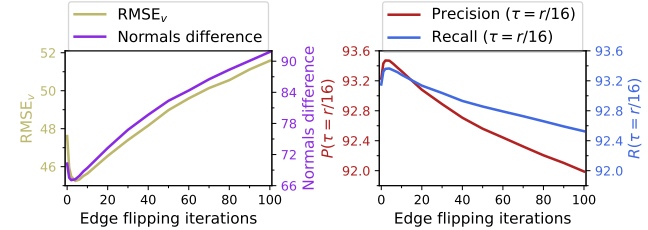


Figure 3. Empirically, only a few (2–4) sets of edge flips yield improvements across most measures as meshes during this stage most closely correspond those seen in training set.

a simplified scheme inspired by [34]. Any edits violating these invariants are discarded in each iteration before applying them to the input mesh. Figure 2 presents an overview of steps in our remeshing procedure, described below.

**Patch Extraction.** We densely extract local, overlapping triangulated patches  $P_i$  of up to  $n_v = 2000$  vertices from the input mesh. Local feature estimation allows our method to scale effectively to arbitrarily large meshes. The overlap across patches serves as a form of test-time augmentation [66], enhancing the robustness of our approach.

**Patch-Based Feature Estimation and Fusion.** We use the trained networks  $f_d, f_r$  to predict a scalar distance-to-feature field  $\hat{d}_i^{\varepsilon}$  and a vector direction-to-feature field  $\hat{r}_i^{\varepsilon}$  at vertices  $V = \{v\}$  in each patch  $P_i$ . We fuse per-patch predictions to reconstruct the shape-level feature-aware fields.

**Snapping Vertices to Features.** Assuming that smooth surface regions are well approximated by the mesh extraction method (*e.g.*, MC33 [45, 50]), we focus on optimizing per-point and normals deviations in regions proximal to features. For per-point deviations captured by  $\hat{d}^{\varepsilon}$ , we identify vertices predicted to be near sharp features (vertices  $v$  with  $\hat{d}^{\varepsilon}(v) \leq \alpha_{\text{prox}} = 2\lambda$ ) and move them according to the *vertex snapping* rule:  $v \leftarrow v + \hat{d}^{\varepsilon}(v) \cdot \hat{r}^{\varepsilon}(v)$ . This vertex update can be understood as a gradient descent step for minimizing  $\sum_v \hat{d}^{\varepsilon}(v)$ , with  $\hat{r}^{\varepsilon}$  playing the role of the negative gradient and  $\hat{d}^{\varepsilon}$  the role of the magnitude. Some vertex updates violate invariants and are discarded in accordance with the general framework. While this procedure already reconstructs features and reduces per-point deviations, the resulting mesh may still exhibit irregular triangle orientations. To address this, we perform the following two steps.

**Patch-Based Surface Improvement and Fusion.** We reconstruct the surface improvement field  $\hat{s}$  at edges in the complete mesh by predicting local fields  $\hat{s}_i$  in each snapped patch  $P_i$  using our surface improvement net  $f_s$  and averaging predictions across overlapping patches.

**Interleaved Remeshing and Re-evaluation.** To optimize surface orientation as evaluated by  $\hat{s}$ , we keep the vertices in the coarse mesh fixed. We then select a subset of  $n_{\text{flip}}$  edges in  $E$  that are (1) predicted to yield maximal surface improvement and (2) exhibit no influence on one another (*i.e.*, flipping an edge  $e_i$  from the set should not affect the

	Method	$P^\infty \uparrow$	$R^\infty \uparrow$	$F^\infty \uparrow$	$P_N^\infty \uparrow$	$R_N^\infty \uparrow$	$F_N^\infty \uparrow$	$P^{2\lambda} \uparrow$	$R^{2\lambda} \uparrow$	$F^{2\lambda} \uparrow$	$P_N^{2\lambda} \uparrow$	$R_N^{2\lambda} \uparrow$	$F_N^{2\lambda} \uparrow$	$RMSE_v \downarrow$	$LPIPS_v \downarrow$	#F
Voxel resolution: $128^3$	MC33 [41]	96.5	95.2	95.8	95.2	94.3	94.8	78.6	72.1	75.2	71.8	67.5	69.5	79.5	117.2	$1\times$
	EMC [38]	95.3	94.1	94.7	93.7	92.9	93.3	71.9	66.1	68.9	62.8	59.1	60.9	83.5	144.3	$2\times$
	NMC [12]	<b>99</b>	<b>98.7</b>	<b>98.8</b>	91.5	95.3	93.4	<b>94.2</b>	<b>92.7</b>	<b>93.4</b>	78.5	82.4	80.4	62.1	296.8	$6.5\times$
	NDC [13]	<u>98.2</u>	<u>98.3</u>	<u>98.3</u>	<u>97</u>	<u>97.3</u>	<u>97.2</u>	90.9	90.8	90.8	85.8	<u>86.8</u>	<u>86.3</u>	<u>52.7</u>	233	$1\times$
	MC33 + GNF [81]	89.1	88.1	88.6	<u>97</u>	96.9	<u>97</u>	39.8	36.9	38.3	<u>86.3</u>	85.6	85.9	66.1	<u>104.3</u>	$1\times$
	MC33 + GCND [58]	93.7	92.3	93	94.2	94.7	94.4	63.2	57.4	60.2	73.9	71	72.4	73.2	162.8	$1\times$
Voxel resolution: $512^3$	Ours	97.4	97.5	97.5	<b>97.8</b>	<b>98</b>	<b>97.9</b>	91.7	91.4	91.6	<b>92.1</b>	<b>92.9</b>	<b>92.5</b>	42.7	<b>101.8</b>	<b>0.3\times</b>
	Method	$P^\infty \uparrow$	$R^\infty \uparrow$	$F^\infty \uparrow$	$P_N^\infty \uparrow$	$R_N^\infty \uparrow$	$F_N^\infty \uparrow$	$P^{2\lambda} \uparrow$	$R^{2\lambda} \uparrow$	$F^{2\lambda} \uparrow$	$P_N^{2\lambda} \uparrow$	$R_N^{2\lambda} \uparrow$	$F_N^{2\lambda} \uparrow$	$RMSE_v \downarrow$	$LPIPS_v \downarrow$	#F
	MC33 [41]	<b>99</b>	<b>98.6</b>	<b>98.8</b>	98.6	98.4	98.5	<b>78.9</b>	<b>71.7</b>	<b>75.1</b>	71.8	66.8	69.2	40.6	<u>105.1</u>	$1\times$
	NMC [12]*	61.7	61.5	61.6	94.4	94.8	94.6	28.1	25.4	26.7	52.2	52.1	52.1	63.6	386.8	$0.4\times$
	NDC [13]*	80.4	80.5	80.4	95.6	95.7	95.6	33.2	30.6	31.8	60.8	67.9	64.1	57	287.9	<b>0.06\times</b>
	MC33 + GNF [81]	96.9	96.6	96.7	<u>99.3</u>	<u>99.3</u>	<u>99.3</u>	41	37.9	39.4	<u>88.3</u>	<u>87.5</u>	<u>87.9</u>	<u>33.6</u>	118.4	$1\times$
Voxel resolution: $512^3$	MC33 + GCND [58]**	98.2	97.9	98.1	97.4	98.6	98	63.8	57.4	60.4	74.6	71.4	73	37.5	217.2	$1\times$
	Ours	<b>99.3</b>	<b>99.4</b>	<b>99.4</b>	<b>99.4</b>	<b>99.5</b>	<b>99.5</b>	<b>90.1</b>	<b>90.3</b>	<b>90.2</b>	<b>90.1</b>	<b>91.7</b>	<b>90.9</b>	24.2	<b>91.7</b>	$0.3\times$

Table 2. Quantitative evaluation of mesh extraction and re-meshing performance for datasets of meshes extracted from exact SDF sampled over  $128^3$  and  $512^3$  volumetric grids. Distance- and normals-based Precision, Recall, and F-score are in percentages where higher values correspond to better results. Measures marked with the superscript “ $2\lambda$ ” are computed over areas within  $2\lambda$  to features. A threshold  $\lambda/16$  is used for computing distance-based measures, and a threshold of  $10^\circ$  for computing normals-based measures.  $RMSE_v$  and  $LPIPS_v$  are in thousandths; their lower values mean better results. The best result is in bold, the second best is underlined.

\* For NMC [12] and NDC [13], output meshes have been computed at their highest available resolution,  $128^3$ ;

\*\* GCND [65] produced corrupted output for 93 out of 167 meshes, we give results for the 74 valid meshes.

estimates  $\hat{s}(e_j)$  if  $i \neq j$ ). Then we perform all allowed flips. These steps are repeated until all edges with a non-negligible surface improvement value (0.01) are flipped, or a maximum number of iterations is reached. Following this, we re-estimate an updated surface improvement across the complete coarse mesh. This process can be seen as a simplified version of discrete, combinatorial minimization of an energy function of the form  $\sum_{e \in E} \hat{s}(e)$ .

**Postprocessing.** We finally perform a simple but effective postprocessing step. For triangles oriented differently to all three of their edge-sharing neighbors, we try flipping each edge to find if this improves alignment w.r.t. neighbors; if so, we keep the flip in the final result.

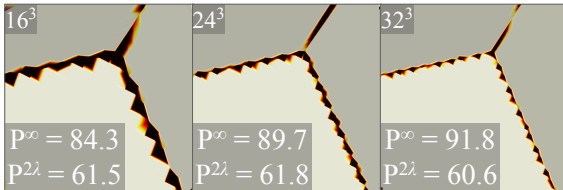


Figure 4. Increasing volumetric resolution reduces but not eliminates aliasing. Global measures (Precision  $P^\infty$ ) are strongly influenced by resolution and therefore unsuitable for capturing feature remeshing performance. In contrast, our measures (Precision  $P^2\lambda$ ) focus on features and only subtly changes with resolution for aliased meshes.

## 5. Experimental Evaluation

**Data and Training.** We train and evaluate our method using high-quality, feature-aligned shapes in the ABC dataset [43], following Sec. 3.1 to compute SDF values and

extract coarse meshes. For training, we sample 36K training, 9K validation, and 5K testing patches, from 761 unique shapes. For evaluation, we create two object-level datasets of 159 meshes extracted from  $128^3$  volumetric SDF and 167 meshes extracted from high-resolution  $512^3$  volumetric SDF. Distance-/direction-to-feature networks are optimized on patches with 500 and 2K vertices using 16 V100 GPUs; the surface improvement network is trained on patches with 500 vertices using 4 V100 GPUs; all three models were trained for 2-3 days, using early stopping. We use Adam [40] with a learning rate  $10^{-3}$  and exponential decay.

**Metrics.** To capture reconstruction accuracy and completeness globally, we respectively use Precision (P) and Recall (R) as commonly done for evaluating 3D reconstruction [41, 79]; to quantify per-face orientation similarity between meshes, we also compute Normals Precision ( $P_N$ ) and Recall ( $R_N$ ). These measures may become less informative at high voxel resolutions (*cf.* Figure 4); we thus present values globally over the entire mesh, and separately over regions within a distance  $\delta \propto \lambda$  to GT sharp geometric features. We report F-scores (F, harmonic means of the pairs of respective values) as aggregate quantities. These measures are superscripted by either  $\infty$  or  $\delta$  (with  $\delta = 2\lambda$ ). For assessing the perceptual quality of reconstructions in comparison to GT meshes, we generate shaded renders from 32 viewing directions under 6 distinct illuminations and compute perceptual  $RMSE_v$  [78] and  $LPIPS_v$  [92] measures.

We assess feature estimation performance by computing Recall( $1\lambda$ ) and FPR( $1\lambda$ ) (False Positives Rate) between true and estimated distance-to-feature values. Similarly, we

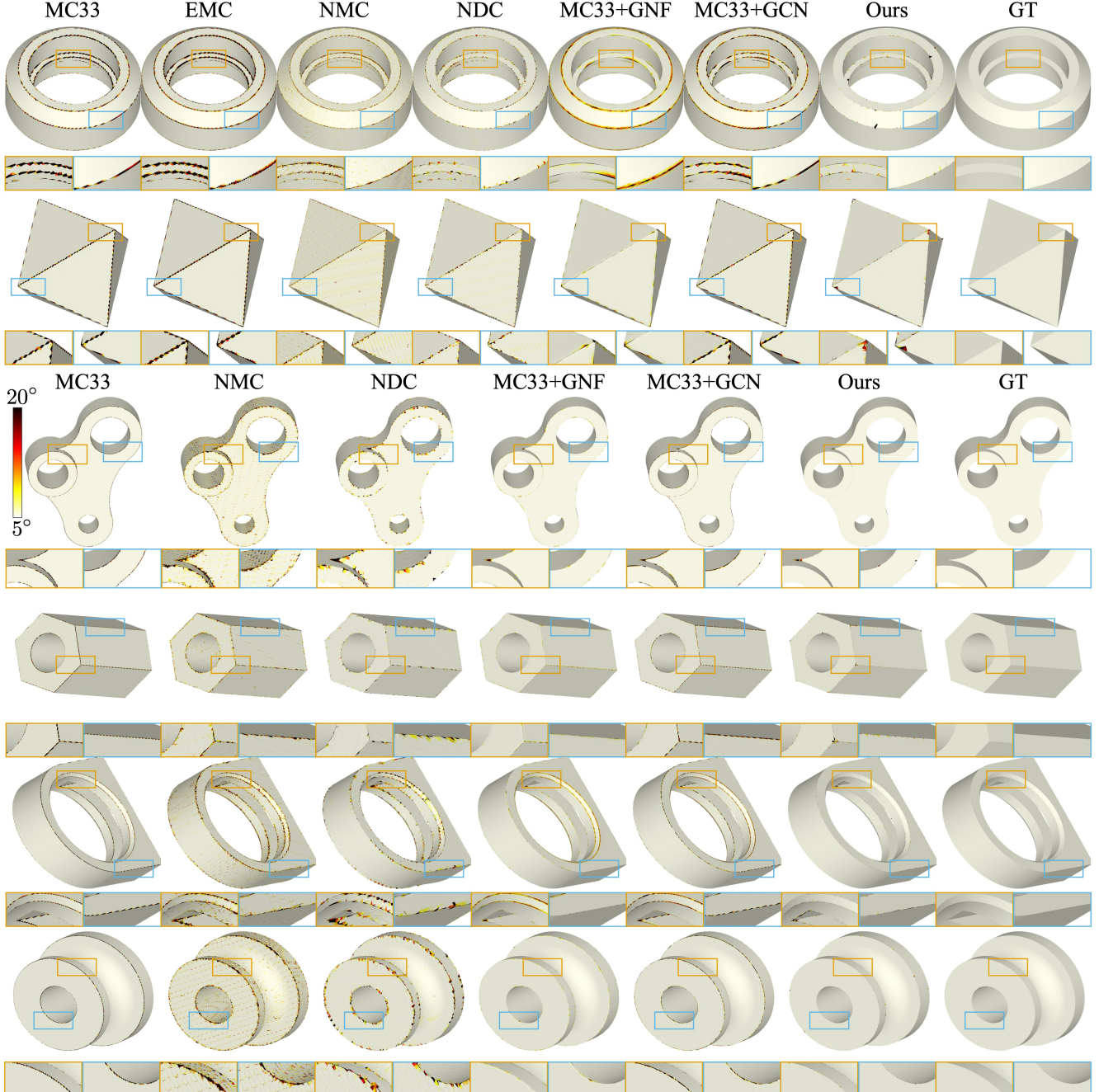


Figure 5. Qualitative reconstruction and re-meshing results for meshes extracted from SDFs sampled over  $128^3$  (top two rows) and  $512^3$  (bottom five rows) volumetric grids. We color predictions by pointwise normals difference between samples on reconstructions and their closest points on GT meshes, clipping these values to the range  $[5^\circ, 20^\circ]$ . Lighter colors correspond to better results. Best viewed in zoom.

calculate  $\text{Recall}(10^\circ)$  and  $\text{FPR}(10^\circ)$  between true and estimated per-vertex direction-to-feature values. To better understand their impact on vertex snapping performance, we conduct remeshing and compute mesh-based measures.

**Baselines.** We compare our method to four mesh extraction algorithms. MC33 [45] is a standard trilinear interpolation-based, local iso-surfacing method. EMC [42] is a feature-sensitive iso-surfacing algorithm relying on edge detection

through angle thresholding, with a threshold set at  $30^\circ$ . NMC [12] and NDC [13] are state-of-the-art learnable methods for mesh extraction from volume data, implementing trained versions of marching cubes and dual contouring, respectively, executed at the highest resolution they have been trained on ( $128^3$ ). In addition, we compare our method to combinations of MC33 with two feature-preserving mesh denoising approaches. GNF [93] is a rep-

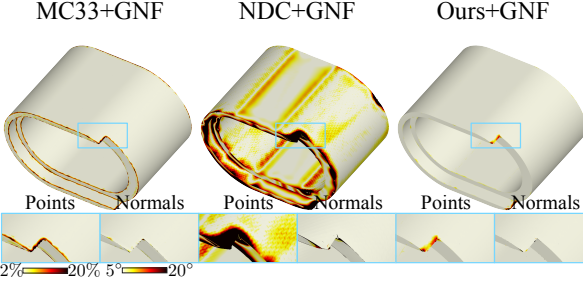


Figure 6. Qualitative mesh smoothing results. Color corresponds to pointwise distances from reconstruction to GT mesh.

Method	$P^{2\lambda}\uparrow$	$R^{2\lambda}\uparrow$	$F^{2\lambda}\uparrow$	$P_N^{2\lambda}\uparrow$	$R_N^{2\lambda}\uparrow$	$F_N^{2\lambda}\uparrow$	$RMSE_v\downarrow$	$LPIPS_v\downarrow$
MC33 [41] + GNF [81]	40.9	37.9	39.4	88.5	87.7	88.1	33.3	119.6
NDC [13] + GNF [81]	29.2	27.9	28.5	81.7	84.8	83.2	41	103.4
Ours + GNF [81]	86	85.7	85.8	96.5	96.5	96.5	19.7	92.1

Table 3. Quantitative evaluation of mesh smoothing performance for a dataset of meshes extracted from  $512^3$  volumetric SDF.

representative normal filtering-based mesh smoothing method, and GCN-Denoiser (GCND) [65] is a state-of-the-art two-stage denoising method integrating GCNs for normal and vertex updating. We run both methods with default parameter settings.

**Can we improve mesh extraction results?** We start by assessing the performance of our framework against mesh extraction baselines, comparing meshes produced by these methods with our remeshing results. Quantitative results are provided in Tab. 2, and visual examples are displayed in Figure 5. For shapes extracted at  $128^3$  resolution, our method outperforms all baselines across all normals-based and perceptual performance measures ( $F_N^\infty$ ,  $F_N^{2\lambda}$ ,  $RMSE_v$ , and  $LPIPS_v$ ). In particular, improvement over the best mesh extraction method NDC constitutes 6.2% in terms of  $F_N^\infty$  and a relative 19% in terms of the perceptual  $RMSE_v$ . Note that our method uses  $3\times$  fewer triangles on average.

For  $512^3$ , our method outperforms all methods across all measures. Specifically, our method improves upon NDC by 19% in terms of  $F^\infty$  and by 58.4% near features in terms of  $F^{2\lambda}$ . Postprocessing MC33 extractions by GNF or GCND produces smoother surfaces (as reflected in  $F_N^{2\lambda}$ ) but sacrifices fidelity to the input mesh, trading pointwise for orientation accuracy. Our method outperforms both GNF and GCND on normals and perceptual measures (e.g., by a relative 22.6% and 57.8%  $LPIPS_v$ , respectively).

**Can our algorithm improve mesh smoothing results?** We study whether reconstructing more accurate geometric features by our refinement step contributes to the performance of subsequent vertex-normal filtering. We apply GNF to meshes obtained by the standard MC33, the state-of-the-art NDC, and the standard MC33 refined by our algorithm. We present statistical results for a dataset of 162 high-resolution ( $512^3$ ) meshes in Tab. 3. We find that while mesh filtering enhances results on MC33 and NDC in terms of normals-based and perceptual measures, it struggles to fully recover sharp features due to severe aliasing in both

Method	$P^{2\lambda}\uparrow$	$R^{2\lambda}\uparrow$	$F^{2\lambda}\uparrow$	$P_N^{2\lambda}\uparrow$	$R_N^{2\lambda}\uparrow$	$F_N^{2\lambda}\uparrow$	$RMSE_v\downarrow$	$LPIPS_v\downarrow$
Ours w/o flips & post	89.7	89.9	89.8	89.4	91.1	90.2	27.1	97.7
Ours w/o post	89.9	90.1	90	89.8	91.5	90.6	26.1	96.4
Ours	90	90.3	90.2	90.1	91.7	90.9	24.3	92.3

Table 4. Quantitative evaluation of contributions of the stages in our algorithm to the final performance for a dataset of meshes extracted from  $512^3$  volumetric SDF.

baselines. Our basic method (no GNF filtering) outperforms MC33, NDC, and MC33 + GNF in terms of  $F_N^{2\lambda}$  (Tab. 2). Tab. 3 and Figure 6 demonstrate that adding smoothing improves our results further.

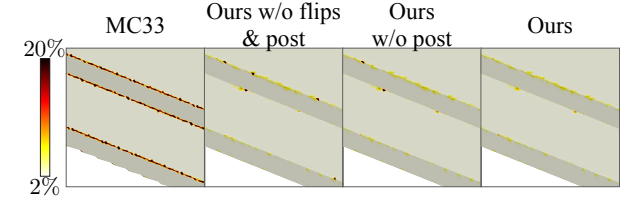


Figure 7. Qualitative ablation results. We color predictions by pointwise distances from reconstruction to GT mesh.

**Which ingredients are essential for achieving good performance?** Critical design choices for our method include (a) the data generation strategy, (b) the learning architecture, and (c) the remeshing strategy. Data-wise, larger patch sizes (2K vs. 500 vertices), denser voxel grids, and aggressive edge collapses prove critical, see Tab. 1. Learning-wise, remeshing performance is improved if the logarithmic scale is used for distances and Laplacian smoothing (Sec. 3.2); edge-based MeshCNN compares favorably to DGCNN adapted to operate on edges. For remeshing, vertex snapping, edge-flipping, and postprocessing all contribute to performance: adding flips and postprocessing increases  $LPIPS_v$  by a relative 5.5%, see Tab. 4 and the visual result in Figure 7. We perform 2 sets of flips in our flipping stage and display the influence of further sets in Figure 3.

We additionally demonstrate a remeshed result for a high-resolution but aliased mesh from ShapeNet [10] in Figure 8.

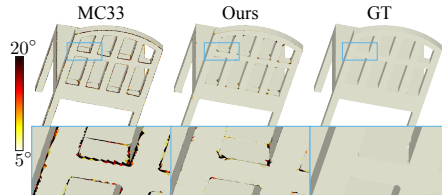


Figure 8. Generalization to ShapeNet [10]. Color corresponds to normals difference between points reconstruction and GT mesh.

## 6. Conclusion

We described a learning-based approach to feature reconstruction and remeshing that operates directly on surface 3D meshes, automatically detects sharp features in the mesh, and scales to arbitrary resolution meshes. Our method trains local patch-based neural models of feature-aware fields defined on the mesh and integrates these into a local remesh-

ing approach as surface-based priors. Compared to state-of-the-art mesh extraction and feature-preserving mesh denoising methods, our method significantly improves surface extraction quality according to normals-based and perceptual quality measures, particularly near features.

## 7. Acknowledgements

The authors acknowledge the use of Skoltech supercomputer Zhores [91] for obtaining the results presented in this paper. The work was supported by the Analytical center under the RF Government (subsidy agreement 000000D730321P5Q0002, Grant No. 70-2021-00145 02.11.2021).

## Appendix

### A. Details on Data Construction

**Adaptive Sampling Distance.** To accurately represent fine-grained features in high-resolution 3D shapes (*e.g.*, thin walls), we adapt the resolution of the volumetric grid to the complexity of the reference (ground-truth, GT) mesh. To this end, we start with establishing a measure of complexity for a 3D shape  $S$  by capturing it with a characteristic linear size  $l_S$ . To compute  $l_S$ , we construct a set of all sharp geometric feature curves  $\Gamma_S = \{\gamma \in S\}$  using the GT annotations available in the ABC dataset [43], extract their linear extents

$$l_\gamma = \max_{n \in \{1, 2, 3\}} \{\max_{p \in \gamma} p_n - \min_{q \in \gamma} q_n\},$$

(*i.e.*, for a feature curve inscribed in a  $3 \times 4 \times 5$  bounding-box, 5 will be returned), and compute  $l_S$  via as an  $\alpha_{\text{curve}}$ -quantile of all values  $\{l_\gamma, \gamma \in \Gamma\}$ . The value  $l_S$  thus provides an estimate of the linear size of smaller (but not the smallest) geometric details in the shape  $S$ . As we aim to query SDF values to reference mesh in grid knots spaced  $\lambda$  units apart, and have  $n$  samples where  $n$  is the number of points sampled along a curve, and  $\lambda$  is a sampling distance (both are our method’s parameters), we scale each mesh using the scaling factor  $\beta_S$  determined by the relation  $\lambda n = \beta_S l_S$ .

**Mesh Simplification Details.** Commonly, meshes extracted using iso-surfacing algorithms [42, 45] include large number of small-area triangles (in particular, “needles” and “caps” with at least one angle close to zero or  $\pi$ ). These can be often pruned by either face or edge collapses [29]. In our method, we use an implementation of progressive meshes [29] available in [34] and remove edges to until 33% of input faces remain. Table 1 in the main text lists values 0, 0.5, and 1 for “Collapse” parameter; this refers to collapsing either no edges, half of the shortest edges (leaving 66% of the input faces), or all shortest edges (leaving 33% of the input faces). The last option proves to be the optimal one according to the ablative studies (Table 1).

**Details on Computing Surface Improvement Field.** We compute surface improvement field by approximating the integral in Equation 2 using sampling. Specifically, we densely and uniformly sample both the coarse and the GT meshes, query the closest points on the counterpart mesh, and compute the normals difference. More formally, let  $P_f = \{p_i\}_{i=1}^{n_f}$  be the set of points sampled on the face  $f$  in the coarse mesh. We compute

$$\text{nc}(f) = \frac{1}{n_f} \sum_{i=1}^{n_f} \|n_{\text{crs}}(p_i) - n_{\text{gt}}(q_i)\| \quad (7)$$

where  $q_i = \pi_{c \rightarrow g}(p_i)$  is the closest point to  $p_i$  on the GT surface mesh. To compute edge-based NC measure by weighted averaging  $\text{nc}(e) = w_1 \text{nc}(f_1) + w_2 \text{nc}(f_2)$ , we use weights  $w_i = n_i / (n_1 + n_2), i = 1, 2$  corresponding to the fraction of points sampled on  $f_i, i = 1, 2$ .

**Parameter Specifications.** We use the following parameters to construct coarse meshes:

- Sampling distance  $\lambda = 0.05$  (could be arbitrarily chosen),
- Number of samples per characteristic linear size,  $n = 80$ ,
- The quantile characterizing short geometric feature curves,  $\alpha_{\text{curve}} = 25\%$ ,
- Quantile for shortest edge collapses  $\alpha_{\text{short}}$  is selected to leave 33% of input faces remain,
- Mean inter-seed distance as supplied to Poisson Disk Sampling [7] for seeds during patch cropping,  $\alpha_{\text{patch}} \cdot \lambda, \alpha_{\text{seed}} = 16$ ,
- Patch radius,  $\alpha_{\text{patch}} \cdot \lambda, \alpha_{\text{seed}} = 32$ ,

**Refinement-Based Data Augmentation** is necessary as local mesh editing is inherently an iterative process leading to a gradual distribution shift for local surface patterns. For accurate remeshing, we require our models to operate efficiently on both sets of raw input and partially refined meshes. To this end, we augment our training dataset with meshes resulting from applying a series of vertex snapping and edge flipping operations computed on both ground-truth and predicted guidance fields (Section 4 in the main text).

### B. Details on Learning Configurations

**Learning Architectures for Field Estimators.** We define our learning architecture for distance- and direction-to-feature fields, inspired by DGCNN [83], as a series of parameterized point processing blocks comprised of neighbour queries, local transform, stacked point convolutions, aggregation, and interpolation layers. We have investigated the influence of various factors on the performance of our distance-/direction-to-feature estimators, most importantly, network capacity (depth expressed as number of layer blocks and width expressed as number of convolutional filters), its receptive field (captured by the number  $k$  of nearest neighbours), supervision regime (predicting the two feature-aware fields jointly or independently), and hav-

ing different loss functions. We report the main findings in Table 1 in the main text and supplement them by results concerning the performance of various architectural options in Tab. 5. The best-performing distance-to-feature estimator is trained using a combination of the  $L_2$  loss and the Laplacian smoothing loss, using the supervision from GT distances only, on datasets of size at least 32K patches.

We train our direction-to-feature model using the loss

$$L(d^\varepsilon, \hat{d}^\varepsilon) = \|d^\varepsilon - \hat{d}^\varepsilon\|^2.$$

**Learning Configurations for Surface Improvement Estimators.** We train our models for estimating the edge-based surface improvement field using the surface meshes resulting from snapping vertices to sharp geometric features.

Our basic comparison is between the MeshCNN [24] and the DGCNN [83] neural architectures. To adapt DGCNN to work on edges, we combine representations of two vertices sharing an edge into the edge embedding by averaging. We additionally compare two variants of MeshCNN [24] architecture differing by how much in-network pooling is performed, influencing the efficiency of in-network information flow. The default architectural option pools 2280 input edges down to 600 edges; our final choice for number of edges (1200 edges) is limited by the fact that we are training on patches where pooling boundary edges can lead to undesired behavior for the MeshCNN network. We experimented with the amount of pooling and found that pooling down to 1200 edges performs better than a larger variant (1600 edges) while affecting only interior edges for patches with 2280 input edges. We present the summary of our findings in Tab. 6 and discuss them in Appendix F.

Models for the improvement predictions are trained on the dataset of patches with snapped vertices. We explore two variants for performing vertex snaps, specifically, by using the ground-truth distance- and direction-to-feature fields, and using the predicted fields. After snapping vertices, we compute GT edge-based improvement values by flipping edges and calculating differences in edge-based normals consistency before and after each flip.

To account for class imbalance during training, we perform experiments using weighted binary cross-entropy (WCE) [67] in addition to the default binary cross-entropy (BCE), defining WCE by

$$\text{WCE} = -\frac{1}{N} \sum_{e=1}^N w s_e \log \hat{s}_e + (1 - s_e) \log(1 - \hat{s}_e) \quad (8)$$

where  $w = (N - \sum_n \hat{s}_e) / \sum_n \hat{s}_e$ .

In summary the best configuration was a MeshCNN model with pooling size of 1200, trained on patches with vertices snapped according to the values of GT distance- and direction-to-feature fields, using plain BCE loss.

## C. Details on Mesh Refinement

**Postprocessing Details.** We note that despite our surface improvement field is able to effectively guide the execution of a few (2–4) sets of flips (in each set, as many as possible non-interacting flips are applied), after applying these, the surface may still benefit from further remeshing. However, once the initial sets of flips are applied, predicting further flips becomes an extremely challenging task as the remaining target flips are too few, while meshes (mesh patches) are becoming partially refined. In machine learning terms, we’re facing a grossly unbalanced segmentation task defined on a sampling distribution that has substantial discrepancy w.r.t. the data distribution of training data for predicting edge-flips.

We therefore design a simple, effective non-learnable postprocessing step that relies on the assumption that most vertices are already snapped and most edge-flips already applied. Specifically, we assume that most meshes we consider are formed of smooth regions connected by sharp geometric feature curves, hence, each triangle should have at least one adjacent (*i.e.*, sharing an edge) neighboring triangle with nearly identical normal. If a particular triangle has no such neighbors, we conclude this to be a result of an irregular chamfering and make an attempt to flip one of its edges to improve alignment in normals to the adjacent triangles.

Concretely, we find triangles where the maximum dot-product between normals in the triangle and its adjacent neighbors is below .95, attempt to flip each of its edges, and keep flips that improve the sum of such dot-products computed over all three sides. We perform this operation until no such triangles are left or until all flips become prohibited by invariants.

## D. Experimental Evaluation Details

**Distance-to-Feature Prediction Evaluation.** We specify in detail additional performance measures used to assess the effectiveness of feature estimation. In our evaluation, we reuse the performance measures defined by the recent feature estimation method [51].

- **Recall( $T$ ):** we compute Recall using the thresholded predictions  $\hat{y}_i = \mathbb{1}(\hat{d}_i < T)$  and the thresholded GT distances  $y_i = \mathbb{1}(d_i < T)$  (we set  $T = \lambda$ , where  $\lambda$  is the sampling distance, *i.e.* the linear voxel size). Recall evaluates the percentage of vertices that are both located within the distance  $T$  to the GT feature line and are predicted to be within  $T$  to the feature line.
- **FPR( $T$ ):** we compute the False Positives Rate using the thresholded predictions and report mean FPR across patches or full models. FPR estimates the percentage of vertices predicted to be located within  $T$  to a sharp feature but are actually located outside the distance  $T$  of the GT feature.

Architecture	$k$	Distances		Directions		$F_{\infty} \uparrow$	$FN_{\infty} \uparrow$	$Rec.\infty \uparrow$	$Prec.\infty \uparrow$
		$Rec.(\lambda) \uparrow$	$FPR(\lambda) \downarrow$	$Rec.(10) \uparrow$	$FPR(10) \downarrow$				
d3w64	32	<u>47.3</u>	1.4	<u>53.6</u>	<u>46.4</u>	85.3	92.7	77.8	94.4
d3w64	64	<b>47.6</b>	<u>0.9</u>	51.4	48.6	<u>85.8</u>	<u>93.2</u>	<u>78.2</u>	<u>94.9</u>
d3w64	128	34.0	<b>0.6</b>	<b>64.0</b>	<b>36.0</b>	<b>88.6</b>	<b>97.0</b>	<b>81.0</b>	<b>97.7</b>
d5w128	64	30.4	0.8	<b>70.0</b>	<b>30.0</b>	87.7	95.9	80.4	96.5
d5w128	128	<b>36.2</b>	<b>0.5</b>	62.7	37.3	<b>88.9</b>	<b>97.4</b>	<b>81.3</b>	<b>98.0</b>

Table 5. Quantitative comparison of learning architectures for distance- and directions-to-feature approximation. We report edge-segmentation intersection-over-union (IoU) measure as it faithfully reflects performance for unbalanced two-class classification of surface improvement values. Architecture: we investigate using variants of DGCNN [83] architectures with various depth and width,  $k$ : number of nearest neighbors related to the receptive field of the model.

- $RMSE$ : the root mean squared error between the predicted distances  $\hat{d}(v)$  and the GT distances  $d(v)$ .
- $RMSE_{q95}$ : the 95% quantile value of  $RMSE$  across a set of instances.

We report the mean value of each measure computed across test patches.

**Direction-to-Feature Prediction Evaluation.** We use the following measures to assess performance of direction-to-feature estimation:

- $Recall(T)$ : we use the predicted direction-to-feature values  $\hat{r}(v)$  and their GT counterparts  $r(v)$ , and compute Recall as the percentage of vertices where angular difference between the two values does not exceed  $T$ :  $Recall(T) = |\{v : \arccos(\hat{r}(v), r(v)) < T\}|/|V|$ .
- $FPR(T)$ : for directions, we set  $FPR(T) = 1 - Recall(T)$ .
- $RMSE$ : the root mean squared error between the predicted directions  $\hat{r}(v)$  and the GT directions  $r(v)$ .
- $RMSE_{q95}$ : the 95% quantile value of  $RMSE$  across a set of instances.

We report the mean value of each measure computed across test patches.

**Computing Mesh-based Performance Measures.** All of the mesh-based performance measures that we use are computed by following the same five-step process. Specifically, we

- (1) densely and uniformly sample either the reconstruction or the GT mesh,
- (2) find the closest points on the counterpart mesh,
- (3) for computing resolution-independent measures over regions within the distance  $\delta$  to GT sharp geometric features, we exclude points that are either sampled on the GT mesh outside the distance  $\delta$  to the GT features, or are sampled on the coarse mesh but have their closest points on the GT mesh outside the distance  $\delta$  to the GT features,
- (4) compute Euclidean distances either in 3D or normals space,
- (5) compute percentage of points with respective distances to the counterpart lower than a threshold.

To evaluate our feature estimation method using mesh-

based performance measures, we predict (depending on the configuration) either only distances, only directions, or both distances and directions using the trained network, complement the predicted values by GT quantities where applicable (e.g., if only distances are predicted, then their predictions are supplemented by GT directions), and perform vertex snaps. We then sample points and compute mesh-based metrics as described above, without performing other remeshing operations.

**Implementation Details.** We use Python’s scientific computing frameworks [25, 59, 76] to construct implementations for the data generation, network training, and the remeshing algorithm. We use PyTorch [58] to construct and optimize our deep learning models for sharp feature priors and take advantage of its higher-level neural network API PyTorch Lightning [20] to rapidly implement experimental options. For configuring all learning and remeshing experiments, we use the Hydra framework [88]. To make our framework and comparisons reproducible, we containerize all our code in Docker [52]. For mesh simplification, we use wild-meshing [34]. We also use Point Cloud Utils [85] and Trimesh [17] to implement various operations involving manipulations with triangle meshes and point sampling.

## E. Additional Qualitative Results

We present additional qualitative results for mesh extraction and re-meshing in Figures 9 and 10. We note that our approach consistently produces lower distortion 3D reconstructions as captured by both distance-based and normals-based performance measures.

## F. Additional Ablative Results

**Learning Configurations for Surface Improvement.** Tab. 6 illustrates our search for an optimal configuration for surface improvement estimation. In terms of comparison of various learning architectures, MeshCNN outperforms the edge-based DGCNN variant by 14.5% IoU, indicating that a neural architecture specially designed to operate on edges is more suitable for edge-based estimation

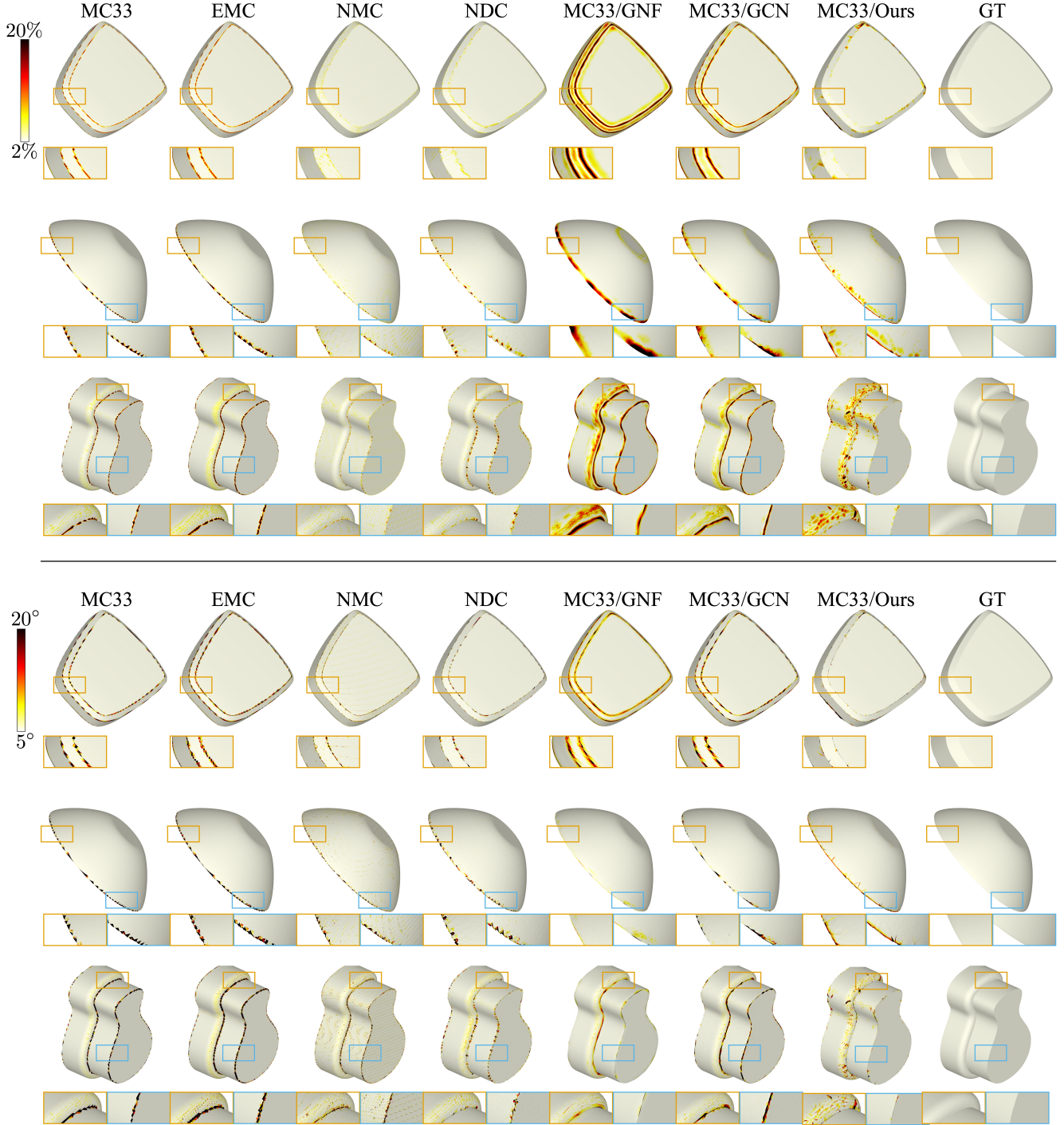


Figure 9. Qualitative reconstruction and re-meshing results for meshes extracted from SDFs sampled over  $128^3$  volumetric grids. In *top three rows*, we color predictions by pointwise distances between samples on reconstructions and their closest points on GT meshes, clipping these values to the range  $[2\%, 20\%]$  relative to  $\lambda$ . In *bottom three rows*, we color predictions by deviation in angle between normals for samples on reconstructions and their closest points on GT meshes, clipping these values to the range  $[5^\circ, 20^\circ]$ . Lighter colors correspond to better results. Best viewed in zoom.

compared to simply “interpolating” quantities from vertices to edges. Since we are using MeshCNN on patches and not full meshes, we were limited on the number of valid pooling operations. We found that pooling patches of size

2280 edges to 1200 edges was optimal, as more pooling resulted in an undefined behavior on patch boundaries, while less pooling leads to 28.5% IoU decrease. Learning with a weighted loss from (8), somewhat surprisingly, did not lead

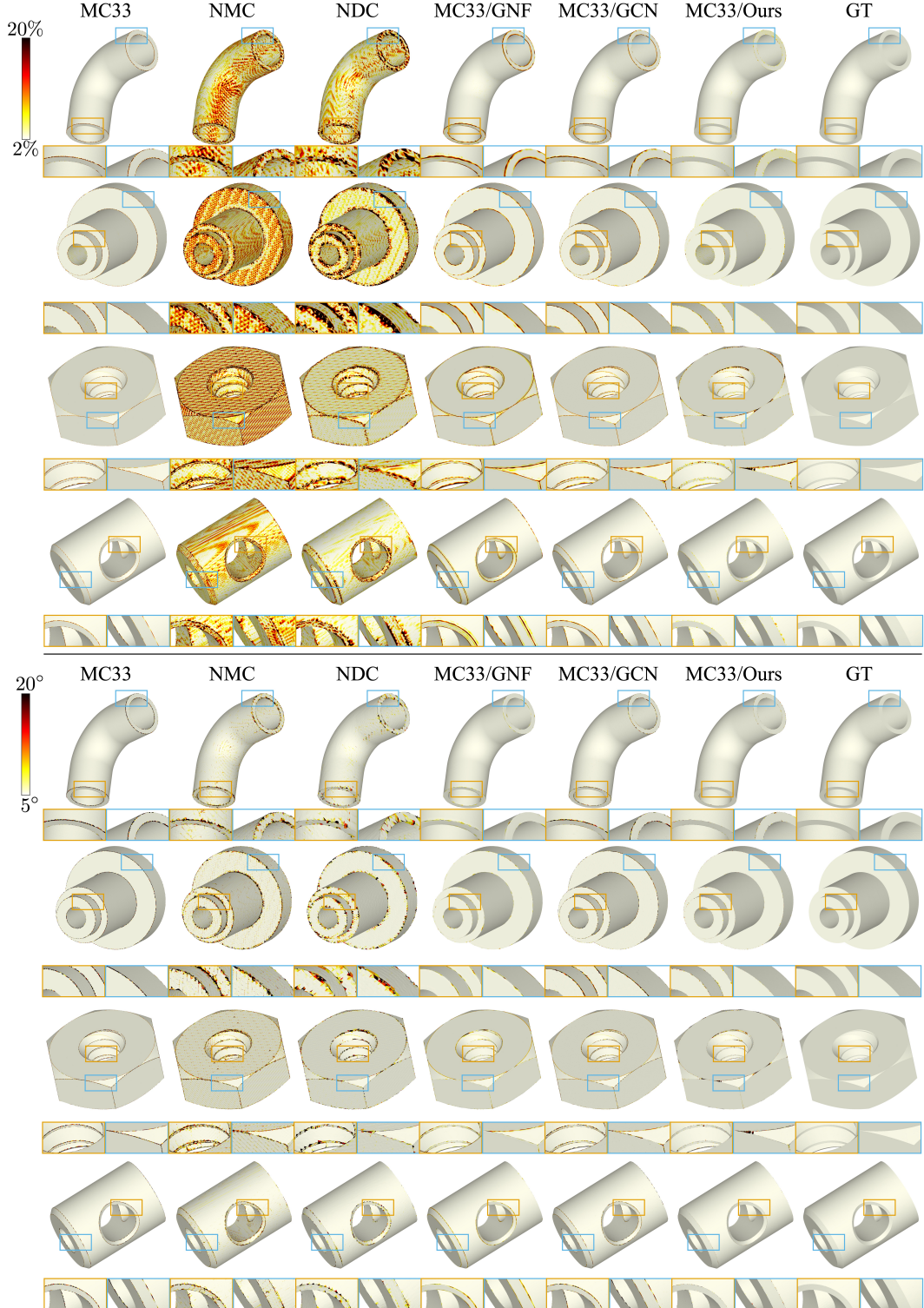


Figure 10. Qualitative reconstruction and re-meshing results for meshes extracted from SDFs sampled over  $512^3$  volumetric grids. In *top three rows*, we color predictions by pointwise distances between samples on reconstructions and their closest points on GT meshes, clipping these values to the range  $[2\%, 20\%]$  relative to  $\lambda$ . In *bottom three rows*, we color predictions by deviation in angle between normals for samples on reconstructions and their closest points on GT meshes, clipping these values to the range  $[5^\circ, 20^\circ]$ . Lighter colors correspond to better results. Best viewed in zoom.

Architecture	Loss	Snap	#P/f.	IoU↑
* MeshCNN, d3p1200	BCE	GT	80	<b>84.8</b>
MeshCNN, d3p1600	BCE	GT	80	56.3
MeshCNN, d3p1200	WCE	GT	80	70.9
MeshCNN, d3p1200	BCE	Pred.	80	61.7
MeshCNN, d3p1200	BCE	GT	8	71.6
DGCNN, d5w128	BCE	GT	80	70.3

Table 6. Quantitative comparison of learning configurations for surface improvement approximation. We report edge-segmentation intersection-over-union (IoU) measure as it faithfully reflects performance for unbalanced two-class classification of surface improvement values. Architecture: we investigate using variants of MeshCNN [24] and DGCNN [83] architectures, Loss: binary (BCE) or weighted (WCE) cross-entropy between predictions and ground-truth segmentation masks, Snap: for vertex snapping, we use either ground-truth (GT) or predicted (Pred.) distance- and direction-to-feature fields, #P/f.: points per feature.

to advantages. In terms of data sources, using GT values of feature-aware fields for performing snapping resulted in 23.1% better IoU scores, presumably due to the spurious snaps negatively impacting the robustness of flips. As with distance- and direction-to-feature fields, larger number of samples per feature resulted in better performance.

**Learning Configurations for Feature Learning.** In Tab. 5, we present quantitative results comparing variants of our DGCNN model. Learning-wise, deeper architectures with larger receptive field achieve better performance; we use  $k = 128$  in our final model.

## References

- [1] Pierre Alliez, Giuliana Ucelli, Craig Gotsman, and Marco Attene. Recent advances in remeshing of surfaces. *Shape analysis and structuring*, pages 53–82, 2008. [2](#) [3](#)
- [2] Matthieu Armando, Jean-Sébastien Franco, and Edmond Boyer. Mesh denoising with facet graph convolutions. *IEEE Transactions on Visualization and Computer Graphics*, 28(8):2999–3012, 2020. [3](#)
- [3] Marco Attene, Bianca Falcidieno, Jaroslaw R Rossignac, and Michela Spagnuolo. Edge-sharpener: recovering sharp features in triangulations of non-adaptively re-meshed surfaces. Technical report, Georgia Institute of Technology, 2003. [3](#)
- [4] Marco Attene, Marcel Campen, and Leif Kobbelt. Polygon mesh repairing: An application perspective. *ACM Computing Surveys (CSUR)*, 45(2):1–33, 2013. [3](#)
- [5] Matthew Berger, Andrea Tagliasacchi, Lee Seversky, Pierre Alliez, Joshua Levine, Andrei Sharf, and Claudio Silva. State of the art in surface reconstruction from point clouds. *Eurographics 2014-State of the Art Reports*, 1(1):161–185, 2014. [2](#)
- [6] Mario Botsch, Leif Kobbelt, Mark Pauly, Pierre Alliez, and Bruno Lévy. *Polygon mesh processing*. CRC press, 2010. [5](#)
- [7] John Bowers, Rui Wang, Li-Yi Wei, and David Maletz. Parallel poisson disk sampling with spectrum analysis on surfaces. *ACM Transactions on Graphics (TOG)*, 29(6):1–10, 2010. [9](#)
- [8] Frédéric Cazals and Joachim Giesen. Delaunay triangulation based surface reconstruction. In *Effective computational geometry for curves and surfaces*, pages 231–276. Springer, 2006. [2](#)
- [9] Rohan Chabra, Jan E Lenssen, Eddy Ilg, Tanner Schmidt, Julian Straub, Steven Lovegrove, and Richard Newcombe. Deep local shapes: Learning local sdf priors for detailed 3d reconstruction. In *European Conference on Computer Vision*, pages 608–625. Springer, 2020. [2](#)
- [10] Angel X Chang, Thomas Funkhouser, Leonidas Guibas, Pat Hanrahan, Qixing Huang, Zimo Li, Silvio Savarese, Manolis Savva, Shuran Song, Hao Su, et al. Shapenet: An information-rich 3d model repository. *arXiv preprint arXiv:1512.03012*, 2015. [8](#)
- [11] Honghua Chen, Mingqiang Wei, and Jun Wang. Geometric and learning-based mesh denoising: A comprehensive survey. *arXiv preprint arXiv:2209.00841*, 2022. [3](#)
- [12] Zhiqin Chen and Hao Zhang. Neural marching cubes. *ACM Transactions on Graphics (TOG)*, 40(6):1–15, 2021. [1](#) [2](#) [3](#) [6](#) [7](#)
- [13] Zhiqin Chen, Andrea Tagliasacchi, Thomas Funkhouser, and Hao Zhang. Neural dual contouring. *ACM Transactions on Graphics (TOG)*, 41(4):1–13, 2022. [1](#) [2](#) [3](#) [6](#) [7](#)
- [14] Zhi-Quan Cheng, Yanzhen Wang, Bao Li, Kai Xu, Gang Dang, and Shiyao Jin. A survey of methods for moving least squares surfaces. In *VG/PBG@ SIGGRAPH*, pages 9–23, 2008. [2](#)
- [15] Evgeny V Chernyaev. Marching cubes 33: Construction of topologically correct isosurfaces. Technical report, 1995. [2](#)
- [16] Keenan Crane, Fernando De Goes, Mathieu Desbrun, and Peter Schröder. Digital geometry processing with discrete exterior calculus. In *ACM SIGGRAPH 2013 Courses*, pages 1–126. 2013. [5](#)
- [17] Dawson-Haggerty et al. trimesh. [11](#)
- [18] Bruno Rodrigues De Araújo, Daniel S Lopes, Pauline Jepp, Joaquim A Jorge, and Brian Wyvill. A survey on implicit surface polygonization. *ACM Computing Surveys (CSUR)*, 47(4):1–39, 2015. [3](#)
- [19] Julie Digne, Jean-Michel Morel, Charyar-Mehdi Souzani, and Claire Lartigue. Scale space meshing of raw data point sets. In *Computer Graphics Forum*, pages 1630–1642. Wiley Online Library, 2011. [2](#)
- [20] WA Falcon. Pytorch lightning. *GitHub. Note: https://github.com/PyTorchLightning/pytorch-lightning*, 3, 2019. [11](#)
- [21] Hanqi Fan, Yizhou Yu, and Qunsheng Peng. Robust feature-preserving mesh denoising based on consistent subneighborhoods. *IEEE Transactions on Visualization and Computer Graphics*, 16(2):312–324, 2009. [3](#)
- [22] Yi-Fei Feng, Li-Yong Shen, Chun-Ming Yuan, and Xin Li. Deep shape representation with sharp feature preservation. *Computer-Aided Design*, page 103468, 2023. [1](#) [3](#)
- [23] André Guéziec and Robert Hummel. Exploiting triangulated surface extraction using tetrahedral decomposition. *IEEE Transactions on visualization and computer graphics*, 1(4):328–342, 1995. [2](#)

[24] Rana Hanocka, Amir Hertz, Noa Fish, Raja Giryes, Shachar Fleishman, and Daniel Cohen-Or. Meshcnn: a network with an edge. *ACM Transactions on Graphics (TOG)*, 38(4):1–12, 2019. [2](#), [3](#), [5](#), [10](#), [14](#)

[25] Charles R Harris, K Jarrod Millman, Stéfan J Van Der Walt, Ralf Gommers, Pauli Virtanen, David Cournapeau, Eric Wieser, Julian Taylor, Sebastian Berg, Nathaniel J Smith, et al. Array programming with numpy. *Nature*, 585(7825):357–362, 2020. [11](#)

[26] Shota Hattori, Tatsuya Yatagawa, Yutaka Otake, and Hiro-masa Suzuki. Learning self-prior for mesh denoising using dual graph convolutional networks. In *Computer Vision–ECCV 2022: 17th European Conference, Tel Aviv, Israel, October 23–27, 2022, Proceedings, Part III*, pages 363–379. Springer, 2022. [1](#)

[27] Klaus Hildebrandt, Konrad Polthier, and Max Wardetzky. Smooth feature lines on surface meshes. In *Symposium on geometry processing*, pages 85–90, 2005. [3](#)

[28] Chems-Eddine Himeur, Thibault Lejemble, Thomas Pellegrini, Mathias Paulin, Loic Barthe, and Nicolas Mellado. Pcednet: A lightweight neural network for fast and interactive edge detection in 3d point clouds. *ACM Transactions on Graphics (TOG)*, 41(1):1–21, 2021. [1](#), [3](#)

[29] Hugues Hoppe. Progressive meshes. In *Proceedings of the 23rd annual conference on Computer graphics and interactive techniques*, pages 99–108, 1996. [5](#), [9](#)

[30] Hugues Hoppe, Tony DeRose, Tom Duchamp, John McDonald, and Werner Stuetzle. Mesh optimization. In *Proceedings of the 20th annual conference on Computer graphics and interactive techniques*, pages 19–26, 1993. [5](#)

[31] Zhangjin Huang, Yuxin Wen, Zihao Wang, Jinjuan Ren, and Kui Jia. Surface reconstruction from point clouds: A survey and a benchmark. *arXiv preprint arXiv:2205.02413*, 2022. [2](#)

[32] Wenzel Jakob, Marco Tarini, Daniele Panozzo, Olga Sorkine-Hornung, et al. Instant field-aligned meshes. *ACM Trans. Graph.*, 34(6):189–1, 2015. [1](#), [3](#)

[33] Chiyu Jiang, Avneesh Sud, Ameesh Makadia, Jingwei Huang, Matthias Nießner, Thomas Funkhouser, et al. Local implicit grid representations for 3d scenes. In *Proceedings of the IEEE/CVF Conference on Computer Vision and Pattern Recognition*, pages 6001–6010, 2020. [2](#)

[34] Zhongshi Jiang, Jiacheng Dai, Yixin Hu, Yunfan Zhou, Jeremie Dumas, Qingnan Zhou, Gurkirat Singh Bajwa, Dennis Zorin, Daniele Panozzo, and Teseo Schneider. Declarative specification for unstructured mesh editing algorithms. *ACM Transactions on Graphics (TOG)*, 41(6):1–14, 2022. [5](#), [9](#), [11](#)

[35] Tao Ju, Frank Losasso, Scott Schaefer, and Joe Warren. Dual contouring of hermite data. In *Proceedings of the 29th annual conference on Computer graphics and interactive techniques*, pages 339–346, 2002. [1](#), [2](#), [3](#)

[36] Evangelos Kalogerakis, Patricio Simari, Derek Nowrouzezahrai, and Karan Singh. Robust statistical estimation of curvature on discretized surfaces. In *Symposium on Geometry Processing*, pages 110–114, 2007. [3](#)

[37] Michael Kazhdan and Hugues Hoppe. Screened poisson surface reconstruction. *ACM Transactions on Graphics (TOG)*, 32(3):1–13, 2013. [2](#)

[38] Alireza Khatamian and Hamid R Arabnia. Survey on 3d surface reconstruction. *Journal of Information Processing Systems*, 12(3):338–357, 2016. [2](#)

[39] Hyun Soo Kim, Han Kyun Choi, and Kwan H Lee. Feature detection of triangular meshes based on tensor voting theory. *Computer-Aided Design*, 41(1):47–58, 2009. [3](#)

[40] Diederik P Kingma and Jimmy Ba. Adam: A method for stochastic optimization. *arXiv preprint arXiv:1412.6980*, 2014. [6](#)

[41] Arno Knapitsch, Jaesik Park, Qian-Yi Zhou, and Vladlen Koltun. Tanks and temples: Benchmarking large-scale scene reconstruction. *ACM Transactions on Graphics (ToG)*, 36(4):1–13, 2017. [6](#)

[42] Leif P Kobbelt, Mario Botsch, Ulrich Schwanecke, and Hans-Peter Seidel. Feature sensitive surface extraction from volume data. In *Proceedings of the 28th annual conference on Computer graphics and interactive techniques*, pages 57–66, 2001. [2](#), [3](#), [7](#), [9](#)

[43] Sebastian Koch, Albert Matveev, Zhongshi Jiang, Francis Williams, Alexey Artemov, Evgeny Burnaev, Marc Alexa, Denis Zorin, and Daniele Panozzo. Abc: A big cad model dataset for geometric deep learning. In *Proceedings of the IEEE Conference on Computer Vision and Pattern Recognition*, pages 9601–9611, 2019. [1](#), [2](#), [3](#), [6](#), [9](#)

[44] Yu-Kun Lai, Qian-Yi Zhou, Shi-Min Hu, Johannes Wallner, and Helmut Pottmann. Robust feature classification and editing. *IEEE Transactions on Visualization and Computer Graphics*, 13(1):34–45, 2006. [3](#)

[45] Thomas Lewiner, Hélio Lopes, Antônio Wilson Vieira, and Geovan Tavares. Efficient implementation of marching cubes’ cases with topological guarantees. *Journal of graphics tools*, 8(2):1–15, 2003. [1](#), [2](#), [3](#), [5](#), [7](#), [9](#)

[46] Xianzhi Li, Lei Zhu, Chi-Wing Fu, and Pheng-Ann Heng. Non-local low-rank normal filtering for mesh denoising. In *Computer Graphics Forum*, pages 155–166. Wiley Online Library, 2018. [3](#)

[47] Xianzhi Li, Ruihui Li, Lei Zhu, Chi-Wing Fu, and Pheng-Ann Heng. Dnf-net: A deep normal filtering network for mesh denoising. *IEEE Transactions on Visualization and Computer Graphics*, 27(10):4060–4072, 2020. [3](#)

[48] Minghua Liu, Xiaoshuai Zhang, and Hao Su. Meshing point clouds with predicted intrinsic-extrinsic ratio guidance. In *European Conference on Computer Vision*, pages 68–84. Springer, 2020. [2](#)

[49] Yujia Liu, Stefano D’Aronco, Konrad Schindler, and Jan Dirk Wegner. Pcw2f: 3d wireframe reconstruction from raw point clouds. In *International Conference on Learning Representations*. [3](#)

[50] William E Lorensen and Harvey E Cline. Marching cubes: A high resolution 3d surface construction algorithm. *ACM siggraph computer graphics*, 21(4):163–169, 1987. [1](#), [2](#), [3](#), [5](#)

[51] Albert Matveev, Ruslan Rakhimov, Alexey Artemov, Gleb Bobrovskikh, Vage Egiazarian, Emil Bogomolov, Daniele Panozzo, Denis Zorin, and Evgeny Burnaev. Def: Deep estimation of sharp geometric features in 3d shapes. *ACM Transactions on Graphics (TOG)*, 41(4):1–22, 2022. [1](#), [3](#), [4](#), [10](#)

[52] Dirk Merkel et al. Docker: lightweight linux containers for consistent development and deployment. *Linux j*, 239(2):2, 2014. 11

[53] Lars Mescheder, Michael Oechsle, Michael Niemeyer, Sebastian Nowozin, and Andreas Geiger. Occupancy networks: Learning 3d reconstruction in function space. In *Proceedings of the IEEE/CVF conference on computer vision and pattern recognition*, pages 4460–4470, 2019. 2

[54] Timothy S Newman and Hong Yi. A survey of the marching cubes algorithm. *Computers & Graphics*, 30(5):854–879, 2006. 3

[55] Yutaka Ohtake, Alexander Belyaev, and Hans-Peter Seidel. Ridge-valley lines on meshes via implicit surface fitting. In *ACM SIGGRAPH 2004 Papers*, pages 609–612. 2004. 3

[56] A Cengiz Öztïrelı, Gael Guennebaud, and Markus Gross. Feature preserving point set surfaces based on non-linear kernel regression. In *Computer graphics forum*, pages 493–501. Wiley Online Library, 2009. 2

[57] Jeong Joon Park, Peter Florence, Julian Straub, Richard Newcombe, and Steven Lovegrove. Deepsdf: Learning continuous signed distance functions for shape representation. In *Proceedings of the IEEE/CVF conference on computer vision and pattern recognition*, pages 165–174, 2019. 2

[58] Adam Paszke, Sam Gross, Francisco Massa, Adam Lerer, James Bradbury, Gregory Chanan, Trevor Killeen, Zeming Lin, Natalia Gimelshein, Luca Antiga, et al. Pytorch: An imperative style, high-performance deep learning library. *Advances in neural information processing systems*, 32, 2019. 11

[59] Fabian Pedregosa, Gaël Varoquaux, Alexandre Gramfort, Vincent Michel, Bertrand Thirion, Olivier Grisel, Mathieu Blondel, Peter Prettenhofer, Ron Weiss, Vincent Dubourg, et al. Scikit-learn: Machine learning in python. *the Journal of machine Learning research*, 12:2825–2830, 2011. 11

[60] Nico Pietroni, Stefano Nuvoli, Thomas Alderighi, Paolo Cignoni, Marco Tarini, et al. Reliable feature-line driven quad-remeshing. *ACM Transactions on Graphics*, 40(4):1–17, 2021. 3

[61] Huamin Qu, Nan Zhang, Ran Shao, Arie Kaufman, and Klaus Mueller. Feature preserving distance fields. In *2004 IEEE Symposium on Volume Visualization and Graphics*, pages 39–46. IEEE, 2004. 3

[62] Marie-Julie Rakotosaona, Paul Guerrero, Noam Aigerman, Niloy J Mitra, and Maks Ovsjanikov. Learning delaunay surface elements for mesh reconstruction. In *Proceedings of the IEEE/CVF Conference on Computer Vision and Pattern Recognition*, pages 22–31, 2021. 2

[63] Michael Schmeling. Averaging correlated data. *Physica Scripta*, 51(6):676, 1995. 5

[64] Nicholas Sharp and Maks Ovsjanikov. Pointtrinet: Learned triangulation of 3d point sets. In *European Conference on Computer Vision*, pages 762–778. Springer, 2020. 2

[65] Yuefan Shen, Hongbo Fu, Zhongshuo Du, Xiang Chen, Evgeny Burnaev, Denis Zorin, Kun Zhou, and Youyi Zheng. Gcn-denoiser: Mesh denoising with graph convolutional networks. *ACM Transactions on Graphics (TOG)*, 41(1):1–14, 2022. 1, 2, 3, 6, 8

[66] Connor Shorten and Taghi M Khoshgoftaar. A survey on image data augmentation for deep learning. *Journal of big data*, 6(1):1–48, 2019. 5

[67] Carole H Sudre, Wenqi Li, Tom Vercauteren, Sébastien Ourselin, and M Jorge Cardoso. Generalised dice overlap as a deep learning loss function for highly unbalanced segmentations. In *Deep Learning in Medical Image Analysis and Multimodal Learning for Clinical Decision Support: Third International Workshop, DLMIA 2017, and 7th International Workshop, ML-CDS 2017, Held in Conjunction with MICCAI 2017, Québec City, QC, Canada, September 14, Proceedings 3*, pages 240–248. Springer, 2017. 10

[68] Xianfang Sun, Paul L Rosin, Ralph Martin, and Frank Langbein. Fast and effective feature-preserving mesh denoising. *IEEE transactions on visualization and computer graphics*, 13(5):925–938, 2007. 3

[69] Vitaly Surazhsky and Craig Gotsman. Explicit surface remeshing. In *Proceedings of the 2003 Eurographics/ACM SIGGRAPH symposium on Geometry processing*, pages 20–30, 2003. 2

[70] Marco Tarini, Nico Pietroni, Paolo Cignoni, Daniele Panozzo, and Enrico Puppo. Practical quad mesh simplification. In *Computer Graphics Forum*, pages 407–418. Wiley Online Library, 2010. 3

[71] Gabriel Taubin et al. Linear anisotropic mesh filtering. *Res. Rep. RC2213 IBM*, 1(4), 2001. 3

[72] E Moscoso Thompson, G Arvanitis, K Moustakas, N Hoang-Xuan, ER Nguyen, M Tran, Thibault Lejemble, Loic Barthe, Nicolas Mellado, C Romanengo, et al. Shrec’19 track: Feature curve extraction on triangle meshes. In *12th EG Workshop 3D Object Retrieval 2019*, pages 1–8, 2019. 3

[73] Maria-Laura Torrente, Silvia Biasotti, and Bianca Falcidieno. Recognition of feature curves on 3d shapes using an algebraic approach to hough transforms. *Pattern Recognition*, 73:111–130, 2018. 3

[74] Graham M Treece, Richard W Prager, and Andrew H Gee. Regularised marching tetrahedra: improved iso-surface extraction. *Computers & Graphics*, 23(4):583–598, 1999. 2

[75] Gokul Varadhan, Shankar Krishnan, Young J Kim, and Dinesh Manocha. Feature-sensitive subdivision and isosurface reconstruction. In *IEEE Visualization, 2003. VIS 2003.*, pages 99–106. IEEE, 2003. 3

[76] Pauli Virtanen, Ralf Gommers, Travis E Oliphant, Matt Haberland, Tyler Reddy, David Cournapeau, Evgeni Burovski, Pearu Peterson, Warren Weckesser, Jonathan Bright, et al. Scipy 1.0: fundamental algorithms for scientific computing in python. *Nature methods*, 17(3):261–272, 2020. 11

[77] Jens Vorsatz, Christian Rössl, Leif P Kobbelt, and H-P Seidel. Feature sensitive remeshing. In *Computer Graphics Forum*, pages 393–401. Wiley Online Library, 2001. 3

[78] Oleg Voynov, Alexey Artemov, Vage Egiazarian, Alexander Notchenko, Gleb Bobrovskikh, Evgeny Burnaev, and Denis Zorin. Perceptual deep depth super-resolution. In *Proceedings of the IEEE/CVF International Conference on Computer Vision*, pages 5653–5663, 2019. 6

[79] Oleg Voynov, Gleb Bobrovskikh, Pavel Karpyshhev, Saveliy Galochkin, Andrei-Timotei Ardelean, Arseniy Bozhenko, Ekaterina Karmanova, Pavel Kopanev, Yaroslav Labutin-Rymsho, Ruslan Rakhimov, et al. Multi-sensor large-scale dataset for multi-view 3d reconstruction. In *Proceedings of the IEEE/CVF Conference on Computer Vision and Pattern Recognition*, pages 21392–21403, 2023. 6

[80] Jun Wang, Xi Zhang, and Zeyun Yu. A cascaded approach for feature-preserving surface mesh denoising. *Computer-Aided Design*, 44(7):597–610, 2012. 3

[81] Peng-Shuai Wang, Yang Liu, and Xin Tong. Mesh denoising via cascaded normal regression. *ACM Trans. Graph.*, 35(6):232–1, 2016. 3

[82] Xiaogang Wang, Yuelang Xu, Kai Xu, Andrea Tagliasacchi, Bin Zhou, Ali Mahdavi-Amiri, and Hao Zhang. Pie-net: Parametric inference of point cloud edges. *Advances in neural information processing systems*, 33:20167–20178, 2020. 1, 3

[83] Yue Wang, Yongbin Sun, Ziwei Liu, Sanjay E Sarma, Michael M Bronstein, and Justin M Solomon. Dynamic graph cnn for learning on point clouds. *Acm Transactions On Graphics (tog)*, 38(5):1–12, 2019. 2, 4, 9, 10, 11, 14

[84] Mingqiang Wei, Jin Huang, Xingyu Xie, Ligang Liu, Jun Wang, and Jing Qin. Mesh denoising guided by patch normal co-filtering via kernel low-rank recovery. *IEEE transactions on visualization and computer graphics*, 25(10):2910–2926, 2018. 1, 3

[85] Francis Williams. Point cloud utils, 2022. <https://www.github.com/fwilliams/point-cloud-utils>. 11

[86] Francis Williams, Zan Gojcic, Sameh Khamis, Denis Zorin, Joan Bruna, Sanja Fidler, and Or Litany. Neural fields as learnable kernels for 3d reconstruction. In *Proceedings of the IEEE/CVF Conference on Computer Vision and Pattern Recognition*, pages 18500–18510, 2022. 2

[87] Rui Xu, Zixiong Wang, Zhiyang Dou, Chen Zong, Shiqing Xin, Mingyan Jiang, Tao Ju, and Changhe Tu. Rfps: Reconstructing feature-line equipped polygonal surface. *ACM Transactions on Graphics (TOG)*, 41(6):1–15, 2022. 1, 3

[88] Omry Yadan. Hydra - a framework for elegantly configuring complex applications. Github, 2019. 11

[89] Sunil Kumar Yadav, Ulrich Reitebuch, and Konrad Polthier. Robust and high fidelity mesh denoising. *IEEE transactions on visualization and computer graphics*, 25(6):2304–2310, 2018. 3

[90] Shin Yoshizawa, Alexander Belyaev, Hideo Yokota, and Hans-Peter Seidel. Fast, robust, and faithful methods for detecting crest lines on meshes. *Computer Aided Geometric Design*, 25(8):545–560, 2008. 3

[91] Igor Zacharov, Rinat Arslanov, Maksim Gunin, Daniil Stefonishin, Andrey Bykov, Sergey Pavlov, Oleg Panarin, Anton Maliutin, Sergey Rykovanov, and Maxim Fedorov. “zhores”—petaflops supercomputer for data-driven modeling, machine learning and artificial intelligence installed in skolkovo institute of science and technology. *Open Engineering*, 9(1):512–520, 2019. 9

[92] Richard Zhang, Phillip Isola, Alexei A Efros, Eli Shechtman, and Oliver Wang. The unreasonable effectiveness of deep features as a perceptual metric. In *Proceedings of the IEEE conference on computer vision and pattern recognition*, pages 586–595, 2018. 6

[93] Wangyu Zhang, Bailin Deng, Juyong Zhang, Sofien Bouaziz, and Ligang Liu. Guided mesh normal filtering. In *Computer Graphics Forum*, pages 23–34. Wiley Online Library, 2015. 1, 2, 3, 7

[94] Yingkui Zhang, Guibao Shen, Qiong Wang, Yinling Qian, Mingqiang Wei, and Jing Qin. Geobi-gnn: geometry-aware bi-domain mesh denoising via graph neural networks. *Computer-Aided Design*, 144:103154, 2022. 3

[95] Wenbo Zhao, Xianming Liu, Yongsen Zhao, Xiaopeng Fan, and Debin Zhao. Normalnet: Learning based guided normal filtering for mesh denoising. *arXiv preprint arXiv:1903.04015*, 2019. 3

[96] Youyi Zheng, Hongbo Fu, Oscar Kin-Chung Au, and Chiwei Lan Tai. Bilateral normal filtering for mesh denoising. *IEEE transactions on visualization and computer graphics*, 17(10):1521–1530, 2010. 3